Local redistribution of dopants and defects induced by annealing in polycrystalline compound semiconductors

V. Consonni,[*] G. Feuillet, and J. P. Barnes

CEA, LETI, MINATEC, 17 rue des Martyrs, 38054 Grenoble Cedex 9, France

F. Donatini

CEA-CNRS-UJF Nanophysics and Semiconductor Group, Institut Louis Néel, 25 rue des Martyrs, 38042 Grenoble Cedex 9, France

The annealing of chlorine-doped polycrystalline CdTe films leads to the occurrence of an abnormal grain structure with the formation of both primary and secondary grains, the latter being larger and growing at the expense of the former. The spatial distribution of dopants and defects has been investigated within both types of grains by time-of-flight secondary-ion-mass spectroscopy imaging and spatially resolved cathodoluminescence. It is found that chlorine atoms similarly segregate in the vicinity of grain boundaries in both primary and secondary grains, whereas chlorine donors are homogeneously distributed away from grain boundaries. It is shown that, contrary to primary grains, secondary grains exhibit specific concentration processes around grain boundaries, such as cadmium vacancy accumulation and dislocation piling up. The existence of long-range stresses around grain boundaries only within secondary grains is also evidenced and attributed to piezoelectric effects. Grain boundaries thus act as getters for dopants and defects by draining them from the interior of secondary grains. These physical mechanisms emphasize efficient purifying effects associated with the beneficial formation and growth of secondary grains within an abnormal grain structure as induced by annealing. The depicted processes can be applied to a wide variety of polycrystalline compound semiconductors and can find direct applications in the field of solar cells based on these materials.

PACS number(s): 78.66.Hf, 78.60.Hk, 61.72.Cc, 61.72.Mm

I. INTRODUCTION

Polycrystalline semiconductors (SCs) have received increasing interest due to their potential use in cost-efficient electronic, optical, and chemical devices where very large dimensions are required, such as solar cells, x- and γ-ray detectors, varistors or gas sensors.[1–3] The growth of polycrystalline SC films follows the Volmer-Weber mechanism, for which isolated three-dimensional islands nucleate at the substrate surface, grow in size and then coalesce.[4,5] Upon island coalescence, grain boundaries (GBs) are formed and high biaxial tensile stresses are generated, contributing to the nucleation of dislocations at the contact point between two adjacent grains.[5] These stresses can be relieved by the transport of impurities into GBs, generating compensating biaxial compressive stresses and inducing segregation processes.[6–8] Such processes can have deleterious effects, resulting in the occurrence of locally nonuniform doping regions.[8] In particular, local probe measurements have highlighted that the GB contribution to the conduction is enhanced but uncontrolled in a wide variety of polycrystalline SCs.[9–17] Island coalescence thus induces the formation of a highly defective and randomly oriented grain structure and appears to be detrimental for the structural properties and for the doping and transport characteristics of polycrystalline SC films.[18]

In order to improve the crystalline quality of these films, in terms of grain-size distribution, columnar morphology and texturation, *ex situ* thermal treatments are usually carried out following deposition. Their effects on the structural properties have widely been investigated for *indirect* band-gap polycrystalline SC films, such as silicon or germanium.[19] We have recently shown that polycrystalline compound SCs, which for most of them are direct band-gap materials, behave in a similar way upon annealing.[20] Indeed, as interface, surface and strain energies are strongly anisotropic for most of these materials, a process of abnormal grain growth occurs upon annealing: it consists in the preferential growth of larger secondary grains at the expense of the smaller primary grain matrix for energetic reasons.[21] However, initial segregation processes induced by island coalescence lead to solute drag phenomena, which prevent secondary grains from consuming the entire primary grain matrix, hence resulting in the formation of a nonuniform grain structure.[22] This inhomogeneous grain structure could have a profound influence on the concentration and spatial distribution of extended and intrinsic point defects as well as of dopants in polycrystalline SC films. The doping and transport properties of the devices based on these materials may, in turn, be affected. Nevertheless, very few works have been devoted to this issue for both *indirect* and *direct* band-gap polycrystalline SC films, due in particular to the absence of dedicated experiments. The aim of this study is to cast a light into the physical mechanisms leading to the specific abnormal grain structure on a local scale and, especially, to reveal their effects on the behavior of dopants and defects in polycrystalline SC films. The aim is also to evidence the role of GBs within these polycrystalline films leading to their very specific properties.

We investigate the structural reordering of polycrystalline SC films upon annealing and correlate it with their doping properties, by benefiting from optical characterization tools commonly used in *direct* band-gap SCs such as photoluminescence and cathodoluminescence (CL) at the macroscopic and local scales, respectively. In the following, we focus on polycrystalline CdTe films but most of our findings can be

applied to a wide variety of polycrystalline compound SCs, especially belonging to the III/V, II/VI, or chalcopyrite groups. To a lesser extent, some similarities can also be found with *indirect* band-gap polycrystalline SCs. Spatially resolved 5 K CL measurements and time-of-flight secondary-ion-mass spectroscopy (ToF-SIMS) imaging are combined so as to carry out the study of the local redistribution of extended and intrinsic point defects as well as of dopants in an abnormal grain structure induced by annealing in polycrystalline CdTe. We specifically address the major differences between primary and secondary grains composing the abnormal grain structure. It is shown that, contrary to primary grains, the interior of secondary grains is almost free of all types of defects, revealing that GBs act as getters for chlorine dopants and cadmium vacancies as well as for dislocations within this type of grains. Stress concentrations around GBs in secondary grains are also evidenced and attributed to piezoelectric effects. These physical mechanisms emphasize the beneficial purifying effects related to the process of abnormal grain growth in polycrystalline compound SC films.

II. EXPERIMENT

20-μm-thick chlorine-doped polycrystalline CdTe samples were grown on graphite substrates by close space sublimation. Chlorine doping was achieved *in situ* by using a source material composed of a mixture of high-purity 5N CdCl$_2$ and CdTe powders, which was evaporated on a graphite substrate located at a distance of about 5 mm. An *in situ* thermal treatment under nitrogen was subsequently performed to generate the abnormal grain structure, at an annealing temperature of 630 °C for 2 h at one atmosphere. 5 K CL measurements were performed with a quanta 200 FEI scanning electron microscope (SEM). 5 K CL spectra were measured with a monochromator coupled to a N$_2$-cooled charge-coupled device. 5 K CL images were obtained with a photomultiplier synchronized with the primary electron-beam scanning. A 10 kV primary electron beam was used as excitation, leading to a pearlike shape interaction volume of 2.5–3.5 μm^3 in CdTe: the equivalent diameter of the probe is about 1.8 μm. The ToF-SIMS images were achieved with a ToF-SIMS apparatus from Iontof: note that the spatial resolution of the apparatus is about 200 nm. Transmission electron microscopy (TEM) images were made with a JEOL 4000EX microscope operating at 400 kV.

III. RESULTS

The abnormal grain structure of annealed chlorine-doped polycrystalline CdTe films consists of two populations of grains, as depicted in the SEM image of Fig. 1: larger secondary grains with diameters of about 20–30 μm are preferentially oriented along the $\langle 100 \rangle$ crystallographic direction and embedded in a randomly oriented matrix of smaller primary grains with diameters of approximately 6–8 μm.[20]

A. The segregation of chlorine atoms around GBs in the abnormal grain structure

ToF-SIMS measurements indicate that the chlorine concentration in the abnormal grain structure is similarly low,
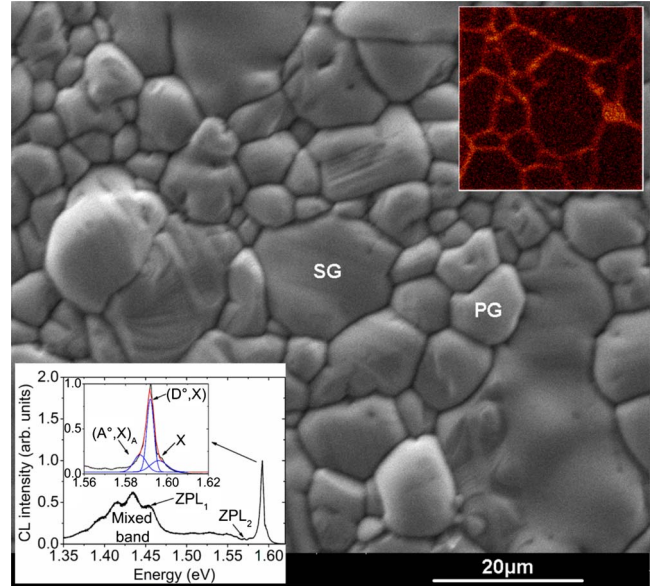

FIG. 1. (Color online) SEM image of the abnormal grain structure composed of larger secondary grains embedded in a smaller primary grain matrix. PG and SG, respectively, stand for the primary grain and the secondary grain in which localized CL spectra are recorded at 5 K in Figs. 3 and 4. The insets show a 45×45 μm^2 ToF-SIMS image of the chlorine signal in the abnormal grain structure and a typical CL spectrum within either primary or secondary grains.

i.e., 1.5×10^{16} at. cm^{-3}, in both primary and secondary grains, as shown in the inset of Fig. 1. Nevertheless, the chlorine spatial distribution is found to be nonuniform: chlorine atoms segregate around GBs, resulting in a chlorine concentration which is four times higher in the vicinity of GBs than in the grain interior. The segregation spreads over 1 μm on each side of GBs and originates from the transport of chlorine atoms into GBs upon island coalescence so as to relieve high biaxial tensile stresses.[6–8,18] The annealing yields a diffusion-induced reduction in chlorine concentration, both within grains themselves and at GBs, as discussed in Ref. 20.

B. The spatial distribution of luminescence in the CdTe abnormal grain structure

The main features of luminescence within primary or secondary grains induced by annealing under nitrogen are revealed in the inset of Fig. 1. The excitonic band is composed of three types of emissions.[20] Radiative recombinations of free excitons X, of excitons bound to chlorine donors, $(D°,X)$, and to chlorine A centers, $(A°,X)$, give rise to three lines at 1.596, 1.5925, and 1.587 eV, respectively.[23–25] In CdTe, chlorine atoms act as hydrogenic donors by substituting for tellurium, Cl$_{Te}$, but can also form chlorine A centers, as (V_{Cd},Cl_{Te}) compensating acceptor complexes.[24,26] Below 1.5 eV, a mixed band is identified between 1.35 and 1.47 eV, consisting of a zero phonon line (ZPL$_1$) centered at 1.46 eV followed by four longitudinal-optical (LO) phonon replicas, each separated by a phonon energy of 21.3 meV.

Such a mixed band is composed of radiative transitions of donor-acceptor pairs involving both Cl_{Te} donors and chlorine A centers, DAP_A, and of excitons bound to extended defects, $(A°, X)_{dis}$.[8,20,26,27] The envelop of the mixed band yields an intermediate value of 1.4 for the Huang-Rhys coupling constant.[8,20] Furthermore, a specific band gives rise to a ZPL_2 at 1.57 eV followed by three LO phonon replicas but it has not been identified yet, although some works assigned it to compensating deep donors.[28] We point out that β acceptor complexes, which supposedly include one cadmium vacancy related to two Cl_{Te} donors, are no longer present after annealing under such conditions.[8,20]

Monochromatic CL images at 1.592 and 1.46 eV are shown in Figs. 2(a) and 2(b) in order to yield the spatial

(a)   20μm


(b)   20μm
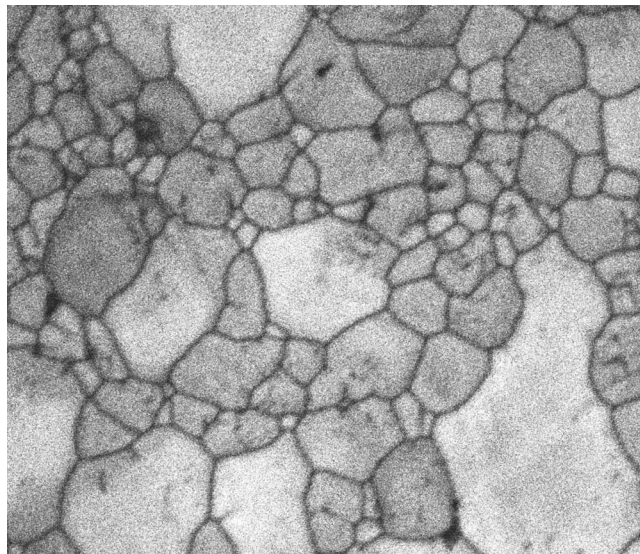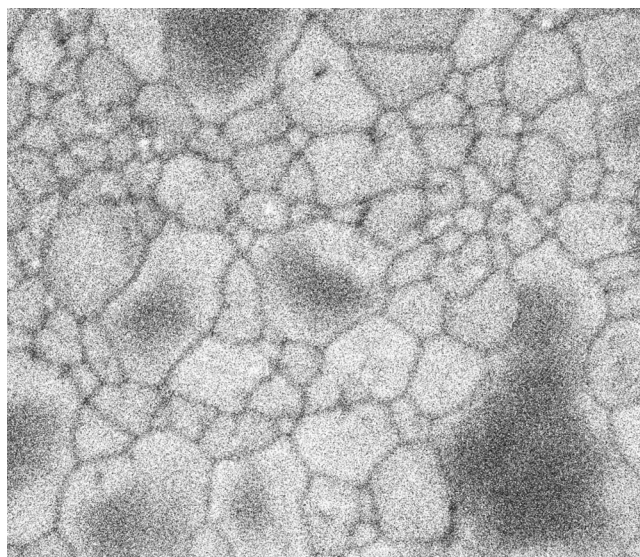
FIG. 2. Monochromatic CL images recorded at 5 K of the same SEM image given in Fig. 1. For (a) and (b), the CL detection energy was chosen to be 1.592 eV (excitonic band) and 1.46 eV (mixed band), respectively. Note that the energy resolution of CL imaging is ±4 meV.

distribution of emissions from the excitonic and mixed bands, respectively. Note that the energy resolution is around ±4 meV for these two monochromatic CL images so that only the free exciton and $(D°, X)$ lines are involved in Fig. 2(a). While grains are the seat of radiative recombinations and correspond to bright regions, GBs appear as preferentially nonradiative recombination centers probably due to the presence of dangling bonds within them.[29] Internal electric fields at GBs can also separate excited electron-hole pairs, resulting in a decrease in the total radiative efficiency as discussed in the following.[9–12] Interestingly, the intensity of the excitonic band is uniform within both primary and secondary grains: this reveals that chlorine atoms and more precisely Cl_{Te} donors are uniformly distributed within both types of grains, as partly evidenced by the ToF-SIMS image in the inset of Fig. 1. However, secondary grains appear much brighter than primary grains: in other words, the excitonic band is thus much more intense in secondary grains than in primary grains. Since the chlorine concentration is identical within the two types of grains according to the ToF-SIMS measurements, we deduce that the density of free excitons within secondary grains is higher than that within primary grains. This is a strong indication that secondary grains present a better crystalline quality with respect to primary grains since free excitons form more easily in materials with low defect densities. We note further that the intensity of the mixed band is uniform within primary grains but nonuniform within secondary grains, as seen in Fig. 2(b): the relative and absolute intensities of the DAP_A and $(A°, X)_{dis}$ lines thus vary according to the spatial position within secondary grains. In order to go into the details of the physical phenomena responsible for the major differences between the two types of grains, spatially resolved 5 K CL spectra are shown below at different spatial positions relative to GBs in both primary and secondary grains.

C. The homogeneous spatial distribution of defects in small primary grains

Five typical spatial positions from the grain interior toward the GB, each separated by a step of 1 μm, are selected in a small primary grain of about 8 μm in diameter and represented by cross icons in the inset of Fig. 3(a). The respective localized 5 K CL spectra are given in Fig. 3. The CL spectra located on the spatial positions numbered from (1) to (3), namely, within the small primary grain away from the GB (i.e., at a distance of more than 1 μm) are strictly similar. Both the overall intensities and shapes of the excitonic band and of the mixed band remain identical within the primary grain: the contribution of the different lines involved in these bands is independent upon the spatial position selected within the primary grain. The spatial distributions of Cl_{Te} donors, of chlorine A centers (i.e., of cadmium vacancies) and of dislocations are thus uniform within the primary grain away from the GB (i.e., at a distance of more than 1 μm). These observations are correlated with the ToF-SIMS and 5 K monochromatic CL images given in Figs. 1 and 2(a), which reveal, in particular, a constant chlorine concentration within primary grains and a segregation region spreading
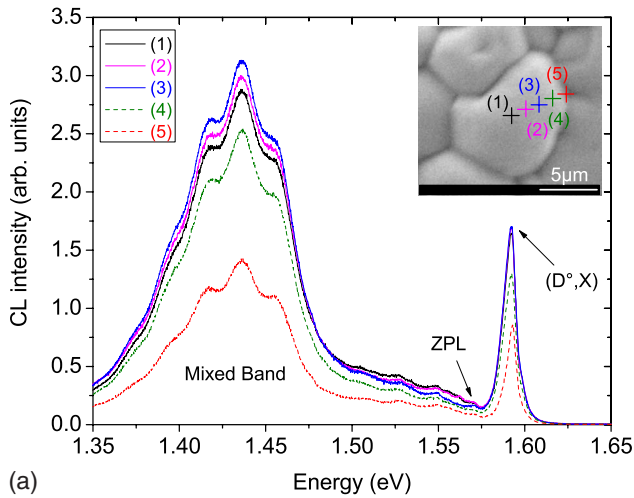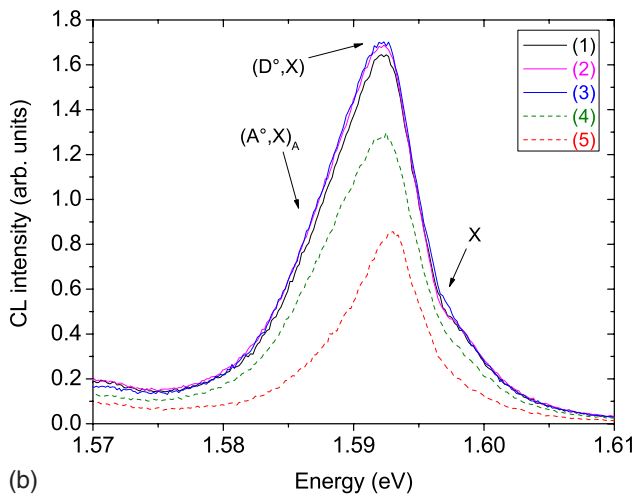
FIG. 3. (Color online) (a) Localized CL spectra recorded at 5 K within a primary grain. The inset shows a direct SEM image of the probed primary grain with different spatial positions represented by cross icons and numbered from (1) to (5) from the grain interior to the GB. (b) Localized CL spectra recorded at 5 K, highlighting the main features of the excitonic band.

over only 1 μm on each side of GBs. In contrast, the intensities of all these bands decrease for the spatial positions numbered (4) and (5), namely, when approaching the GB (i.e., at a distance of less than 1 μm). Indeed, for these spatial positions, the 1.8 μm equivalent diameter of the pearlike electron probe encompasses the GB. The decrease in the total radiative efficiency in the vicinity of the GB is due, in particular, to the presence of nonradiative recombination centers, such as dangling bonds, for instance. As a consequence, we infer that primary grains retain homogeneous spatial distributions of defects and dopants away from GBs (i.e., at a distance of more than 1 μm), which is not the case for secondary grains as detailed below.

### D. The local redistribution of defects in larger secondary grains

1. The accumulation of cadmium vacancies around GBs

Five typical spatial positions from the grain interior toward the GB, each separated by a step of 2 μm, are selected

in a larger secondary grain of about 20 μm in diameter and represented by cross icons in the inset of Fig. 4(a). The respective localized 5 K CL spectra are given in Fig. 4. The intensity of the maximum of the excitonic band, which, as in the case of the primary grain, corresponds to the (D°, X) line, remains constant within the secondary grain away from the GB (i.e., at a distance of more than 1 μm). The spatial distribution of Cl_{Te} donors is thus uniform within the secondary grain away from the GB (i.e., at a distance of more than 1 μm). This observation is again correlated with the ToF-SIMS and 5 K monochromatic CL images shown in Figs. 1 and 2(a). On the contrary, the overall intensity and shape of the excitonic band vary: its asymmetry around 1.587 eV is more and more pronounced from spatial positions numbered (1) to (5), namely, when approaching and reaching the GB. Such an asymmetry is directly related to the presence of the $(A^\circ, X)_A$ line at 1.587 eV. From the fitting procedure of the excitonic band by three Gaussians as described in the inset of
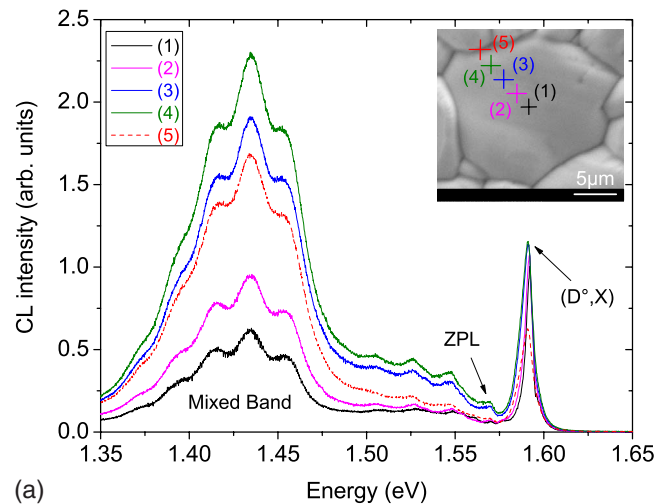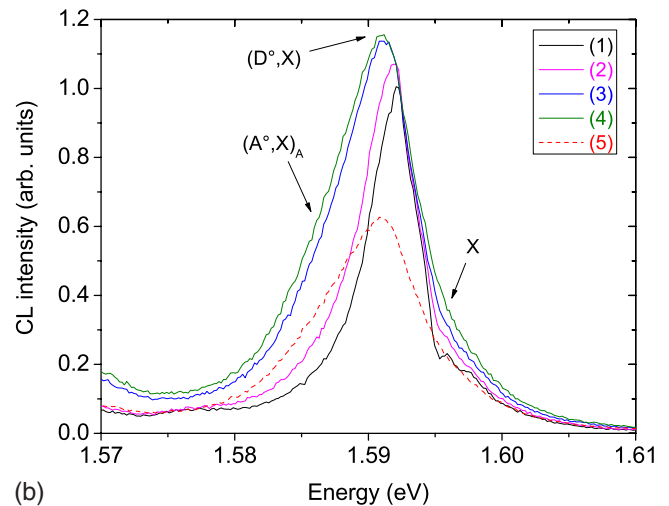
FIG. 4. (Color online) (a) Localized CL spectra recorded at 5 K within a secondary grain. The inset shows a direct SEM image of the probed secondary grain with different spatial positions represented by cross icons and numbered from (1) to (5) from the grain interior to the GB. (b) Localized CL spectra recorded at 5 K, highlighting the main features of the excitonic band.

Fig. 1, we determine the intensity of the $(A^\circ, X)_A$ line by taking the area over the corresponding Gaussian fit. We find that such an intensity continuously increases from spatial positions numbered (1) to (4), as shown in Fig. 5. Concerning the spatial position numbered (5), a decrease in the total radiative efficiency in the vicinity of GBs is again involved, as previously mentioned in the case of primary grains. In other words, the density of chlorine A centers increases when approaching the GB: as Cl_{Te} donors are homogeneously distributed within the secondary grain at a distance of more than 1 μm from the GB, we deduce that the density of cadmium vacancies increases from the grain interior toward the GB. We emphasize further that the accumulation process of cadmium vacancies is effective on a region of several μm around the GB, which is much larger than for the segregation of chlorine atoms. Also, this accumulation process only occurs on one side around the GB exclusively within the secondary grain, whereas the segregation of chlorine atoms is symmetric and proceeds in both sides of the GB in primary and secondary grains.

2. The piling up of dislocations around GBs

The overall intensity of the mixed band increases from spatial positions numbered (1) to (4), namely, within the secondary grain away from the GB (i.e., at a distance of more than 1 μm). Such an increase is obviously directly associated with the increase in the density of chorine A centers. Nevertheless, the intensity ratio between the $(A^\circ, X)_A$ line and the mixed band decreases when approaching the GB, as shown in Fig. 5: this is a strong indication that the mixed band is more and more intense within the secondary grain when coming closer to the GB (i.e., at a distance of more than 1 μm) due to the increase not only in the DAP_A line intensity but also in the $(A^\circ, X)_{dis}$ line intensity. Therefore, we deduce that the dislocation density increases when approaching the GB, which is the sign of an effective recovery mechanism occurring during the process of abnormal grain
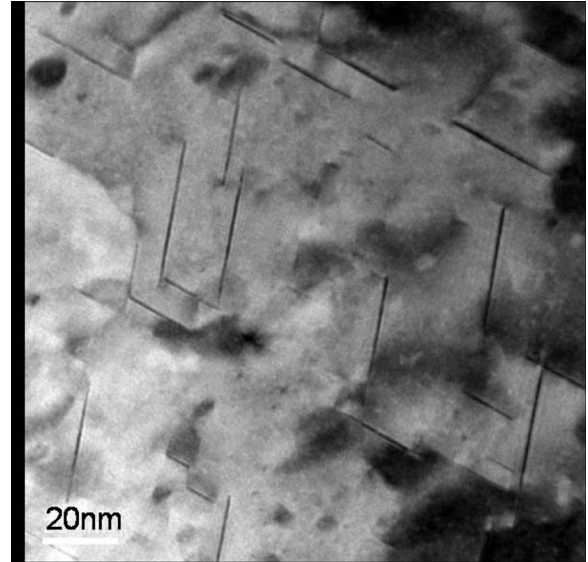
FIG. 6. TEM image within the secondary grain showing stacking faults bounded by Shockley partial dislocations.

growth within secondary grains. Interestingly, this phenomenon is directly observed by TEM imaging. Two different images were taken, one from a region near the GB and the other at a distance of 4 μm within a secondary grain. Stacking faults are clearly visible, bounded by Shockley partial dislocations, as revealed in Fig. 6.[30] From these images, the dislocation density is found to increase by a factor of 1.75 in the vicinity of the GB with respect to the dislocation density at 4 μm, by rising from 460 to 800 μm^{-2}.

3. The occurrence of long-range stresses around GBs

The position of the maximum of the excitonic band shifts toward lower energies when approaching the GB from spatial positions numbered (1) to (5), as revealed in Fig. 4(b). Nevertheless, as the intensities of the three types of emissions involved in the excitonic band vary for these different spatial positions, a fit of the excitonic band by three Gaussians as described in the inset of Fig. 1 is carried out. The position of both (D°, X) and $(A^\circ, X)_A$ lines shifts toward lower energies when approaching the GB, as represented in Fig. 7. Nevertheless, as regards the position of the free exciton line, the accuracy of the fitting procedure is not sufficient to follow its variation precisely. The variation in the energy position is quite similar for these two types of emissions, although a better accuracy is obtained for the (D°, X) line due to its larger intensity. This confirms that such a shift of the excitonic band is not governed by the evolution of the relative intensities for the three types of emissions involved.

In the following, we associate the variation in the energy position for the two distinct lines with stress effects within the secondary grain.[31] The stress magnitude as a function of the distance to the GB is determined by following the energy shift of the (D°, X) line position with respect to its stress-free position at 1.5929 eV, as given by Francou *et al.*[24] Since the absolute value of the stress strongly depends on the reference value selected in the literature, we focus here more on
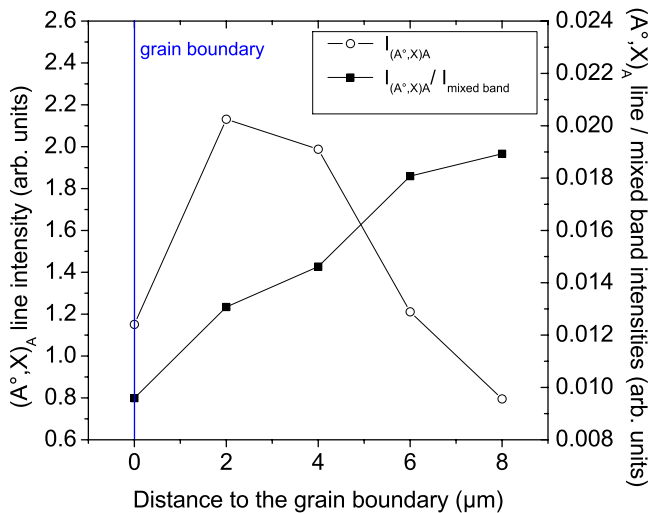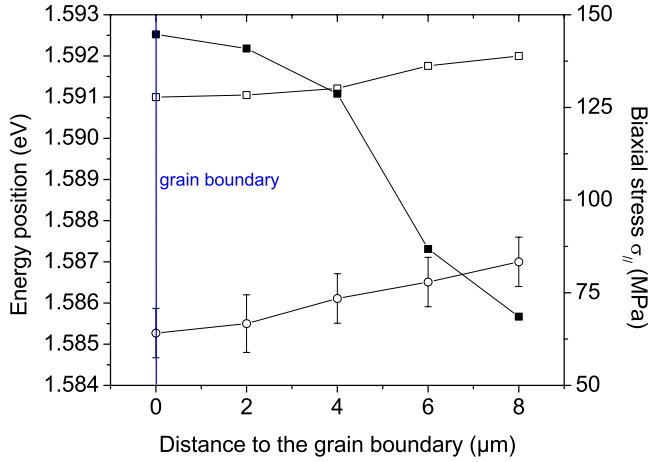

FIG. 5. (Color online) Evolution of the $(A^\circ, X)_A$ line intensity and of its ratio over the mixed band intensity as a function of the distance to the GB in the secondary grain.

FIG. 7. (Color online) Evolution of the energy position for the (D°,X) ($\square$ icons) and $(A^\circ,X)_A$ ($\circ$ icons) lines and of the related biaxial stress ($\blacksquare$ icons) as a function of the distance to the GB in the secondary grain. The error bar of the energy position for the (D°,X) line is ± 0.08 meV.

the relative stress evolution from the grain interior toward the GB. By assuming that the stress state $\sigma_\parallel$ is biaxial within the secondary grain, which is in agreement with previous x-ray diffraction measurements,[18] the hydrostatic and shear stress components induce the following respective variations ΔE_G^{hydro} and ΔE_G^{shear} of the band gap energy[32]

$$\Delta E_G^{hydro} = 2a(s_{11} + 2s_{12})\sigma_\parallel \quad \text{and} \quad \Delta E_G^{shear} = 2b(s_{11} - s_{12})\sigma_\parallel \tag{1}$$

in which a and b are the hydrostatic and shear deformation potentials, equal to -3.85 and -1.235 eV in CdTe (this being an average value between -1.21 and -1.26 eV for the two [100] and [110] crystallographic directions), respectively;[33–35] s_{11} and s_{12} are the compliances equal to 4.254×10^{-11} and -1.734×10^{-11} m^2/N, respectively.[18]

Consequently, the effect of the biaxial stress on the band-gap energy is the following:

$$E_G^{stress} = E_G^{stress\text{-}free} + \Delta E_G^{hydro} - \frac{\Delta E_G^{shear}}{2}. \tag{2}$$

Following Eqs. (1) and (2), the stress magnitude is represented in Fig. 7 together with the energy position of the (D°,X) line from which it is deduced. In the secondary grain, the stress magnitude is about several tens of MPa in the bulk of the secondary grain and increases continuously from the grain interior toward the GB: the stress magnitude at the GB is about twice as strong as in the bulk of the secondary grain. The stress concentration around the GB spreads over $6-8$ μm in the secondary grain. Furthermore, we emphasize that such a stress concentration around GBs is effective only in secondary grains since, in primary grains, the (D°,X) line is found to lie at the same energy position whatever the spatial position considered.

The majority of the theoretical models predict long-range stress concentrations over a maximum of only several hundreds of nanometers around GBs.[36,37] However, CdTe has a

high ionicity of typically more than 0.7 in the Philips ionicity scale and has a high piezoelectric constant of about 0.04 C/m^2.[38–40] GBs are further expected to be electrically active in polycrystalline CdTe, similarly to the more general case of polycrystalline compound SCs.[41] The discrepancy may thus originate from piezoelectric effects, as induced by charge accumulation processes at GBs. The formation of deep levels in the band gap at GBs leads to local bending of the conduction and valence bands, with the occurrence of a built-in electric field and eventually of long-range stresses induced by piezoelectric effects. Furthermore, since, in secondary grains, cadmium vacancies and chlorine dopants are dragged toward the GB, the semiconducting material within the bulk of the grain has a very low residual doping. We can assess, in a first approximation, the width W of the induced space-charge region around the GB by the following relation

$$W = \sqrt{\frac{2\varepsilon_0 \varepsilon_r}{q}\left(\frac{1}{N_D} + \frac{1}{N_A}\right)V_\Phi}, \tag{3}$$

where V_Φ is the potential barrier, N_D and N_A are the donor and acceptor densities, respectively. By taking the following typical values, $N_D = N_A = 10^{14}$ at. cm^{-3}, $V_\Phi = 0.5$ V and $\varepsilon_r = 10.16$, the width of the space-charge region is found to be about 3.4 μm.[9,42] Such a space-charge region around the GB can therefore be broad enough so that the built-in electric field spreads over a large distance, typically of several μm. The piezoelectric nature of CdTe and the deep traps associated with the GBs can thus account for the experimentally observed long-range stresses. In addition, as secondary grains are oriented along the $\langle 100 \rangle$ direction, the large misorientation between secondary and primary grains could also be at the origin of a strong stress field around the GB. Furthermore, previous x-ray microdiffraction experiments in polycrystalline aluminum and copper films have also revealed the presence of highly stressed local regions in individual grains due to specific interactions with their neighboring grains.[43,44]

IV. DISCUSSION

In *direct* band-gap SCs (i.e., compound SCs), the availability of optical characterization tools opens possibilities for the study of the physical mechanisms operating, for instance, in the structural reordering of a polycrystalline matrix upon annealing. We have specifically addressed this issue by using spatially resolved CL measurements in order to study the spatial distribution of extended and intrinsic point defects as well as of dopants in annealed polycrystalline CdTe films. As for most polycrystalline films of elastically anisotropic materials, polycrystalline CdTe films rearrange themselves upon annealing, leading to the formation of the so-called abnormal grain structure. The aim of the study was to identify the major differences between small primary grains and larger secondary grains that comprise such an abnormal grain structure, namely, as regards the behavior of dopants and defects. The role of GBs in such a polycrystalline structure was also evidenced. Our findings are summed up in a schematic in Fig. 8.
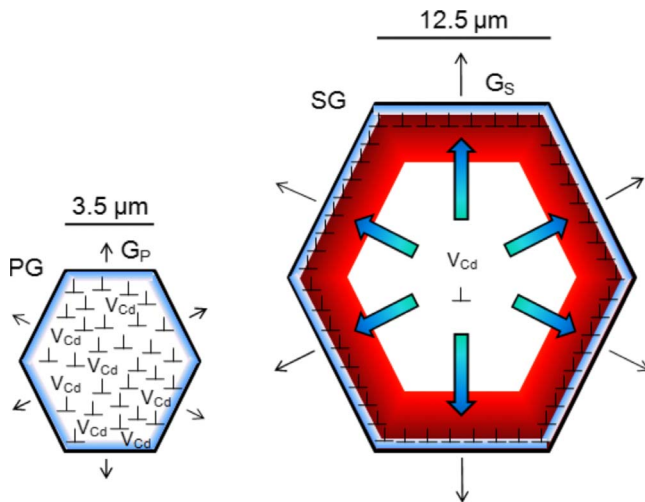
FIG. 8. (Color online) Schematic of the physical mechanisms at work within PG and SG during the process of abnormal grain growth. The blue graded (i.e., light) region represents the chlorine atom segregation around GBs. The red graded (i.e., dark) region symbolizes the stress concentration around GBs. The blue graded arrows represent the cadmium vacancy (V_{Cd}) accumulation around GBs. Cross icons symbolize dislocations and especially their piling up around GBs in SGs. G_P and G_S stand for the growth rate of PGs and of SGs, respectively: $G_P < G_S$ for energetic reasons.

The two types of grains are similar in terms of chlorine doping itself: no difference was found between primary and secondary grains in the ToF-SIMS image of Fig. 1, in which chlorine concentration is low and about 1.5×10^{16} at. cm^{-3}. Chlorine atoms are uniform in the grain interior, i.e., away from the GB at a distance of more than 1 μm. Similarly, Cl_{Te} donors are uniformly distributed in the grain interior within both primary and secondary grains, as revealed by the spatially resolved CL spectra of Figs. 3 and 4. In contrast, the spatial distribution of chlorine is inhomogeneous in the two types of grains when approaching the GBs, with a pronounced segregation in their vicinity, over about 1 μm on each side, as represented by the blue graded (i.e., light) region of Fig. 8 This originates from the transport of chlorine atoms into GBs so as to relieve high tensile biaxial stresses generated upon island coalescence.[6–8,18] The presence of highly doped regions around GBs with respect to the grain interior is expected to change the conductivity type around these extended defects and possibly create embedded p-n junctions within such an abnormal grain structure. Such a process has been reported, for instance, in the case of GBs in polycrystalline ZnO as well as in the case of domain boundaries in monocrystalline ZnO.[14,45,46]

Secondary grains present better structural properties than primary grains in the sense that they are larger with a good morphology and well oriented along the ⟨100⟩ crystallographic direction.[20] Correlatively, the higher intensity of the excitonic band within secondary grains as revealed in Fig. 2(a) is also a strong indication of a better crystalline quality for these grains. Their optical properties are also different from those of primary grains, at least for spatial positions away from GBs at a distance of more than 1 μm and not directly in their center. Primary grains exhibit homogeneous

optical properties, suggesting uniform spatial distribution of dopants and defects within them. We point out that annealing under nitrogen is thus not as beneficial for primary grains as for secondary grains, both in terms of structural and doping properties.[47]

On the contrary, the optical properties of secondary grains are nonuniform. The densities of cadmium vacancies and dislocations are found to continuously increase when approaching the GBs and to be at their maximum at the GBs themselves, as represented by simple cross icons around GBs and blue graded arrows in Fig. 8: in secondary grains, GBs can thus be seen as getters for all types of defects lying originally within the grain interior, contrary to primary grains. Dislocations pile up at GBs, as shown by the spatially resolved CL spectrum and TEM images in Figs. 4(a), 5, and 6. Such a mechanism is the sign of efficient recovery processes within secondary grains.[47] Similarly, chlorine A centers and, as a consequence, cadmium vacancies are also present in higher density in the vicinity of GBs, as revealed by the spatially resolved CL spectrum in Figs. 4(b) and 5. We emphasize that such accumulation processes for cadmium vacancies and dislocations are asymmetric and only appear on one side of GBs within secondary grains, contrary to the segregation of chlorine atoms. They are also effective on a region spreading over several μm on one side of GBs within secondary grains, which is much larger than for the segregation of chlorine atoms. We note that both accumulation processes of cadmium vacancies and dislocations around GBs in secondary grains could be interdependent: some basic works suggest that the annihilation of dislocations in GBs induce the formation of vacancies in order to compensate for the local increase in volume.[48,49] Another view would consist in correlating the dislocation motion toward GBs with cadmium vacancies during a climbing process, for instance. Furthermore, the segregation of chlorine atoms and the accumulation of cadmium vacancies around GBs could drastically influence the kinetics of grain growth for secondary grains: not only can chlorine atoms induce solute drag phenomena but cadmium vacancies could also imply similar processes.[50]

Interestingly, such observations are also made concerning stress concentrations around GBs, which, we believe, arise from piezoelectric effects, as represented by the red graded (i.e., dark) region in Fig. 8. We point out that piezoelectricity is a common physical property of compound SCs:[51–54] such a stress concentration around GBs within secondary grains is thus expected for CdTe and more widely for compound SCs in their polycrystalline variant. Piezoelectric effects around GBs could directly affect the doping and transport properties in these materials.[55] In particular, x-ray microdiffraction experiments are currently in progress in order to correlate such experimental results with direct measurements of the stress tensor around GBs.

V. CONCLUSION

The local redistribution, upon annealing, of cadmium vacancies and dislocations as well as of chlorine dopants has clearly been shown within an abnormal CdTe grain structure composed of larger secondary grains embedded in a matrix

of small primary grains. While the segregation of chlorine atoms in the vicinity of GBs is similar within both types of grains, it is shown that, contrary to primary grains, secondary grains present optimized structural characteristics but inhomogeneous optical properties. This inhomogeneity is due to specific accumulation processes of cadmium vacancies and of dislocations around GBs within secondary grains. As a consequence, GBs can be seen as efficient getters for different types of defects, especially, within secondary grains. Stress concentration around GBs within secondary grains are also found and attributed to piezoelectric effects. These physical mechanisms emphasize beneficial purifying effects associated with the process of abnormal grain growth and occurring within secondary grains. They can be applied to a wide variety of polycrystalline compound SC films, especially belonging to the III/V, II/VI, or chalcopyrite groups, and can find direct applications in the field of solar cells based on these materials.

*Present address: Paul-Drude-Institut für Festkörperelektronik, Hausvogteiplatz 5-7, D-10117 Berlin, Germany.

[1] H. J. Moller, *Semiconductors for Solar Cells* (Artech House, Boston, 1993).

[2] S. M. Sze, *Semiconductor Devices Physics and Technology* (Wiley, New York, 1985).

[3] S. M. Sze, *Semiconductor Sensors* (Wiley, New York, 1994).

[4] M. Volmer and A. Weber, Z. Phys. Chem. **119**, 277 (1926).

[5] C. V. Thompson, Annu. Rev. Mater. Sci. **30**, 159 (2000).

[6] J. A. Floro, S. J. Hearne, J. A. Hunter, P. Kotula, E. Chason, S. C. Seel, and C. V. Thompson, J. Appl. Phys. **89**, 4886 (2001).

[7] E. Chason, B. W. Sheldon, L. B. Freund, J. A. Floro, and S. J. Hearne, Phys. Rev. Lett. **88**, 156103 (2002).

[8] V. Consonni, G. Feuillet, J. Bleuse, and F. Donatini, J. Appl. Phys. **101**, 063522 (2007).

[9] I. Visoly-Fisher, S. R. Cohen, A. Ruzin, and D. Cahen, Appl. Phys. Lett. **82**, 556 (2003).

[10] I. Visoly-Fisher, S. R. Cohen, A. Ruzin, and D. Cahen, Adv. Mater. (Weinheim, Ger.) **16**, 879 (2004).

[11] P. Sutter, E. Sutter, and T. R. Ohno, Appl. Phys. Lett. **84**, 2100 (2004).

[12] S. Smith, P. Zhang, T. Gessert, and A. Mascarenhas, Appl. Phys. Lett. **85**, 3854 (2004).

[13] D. Azulay, O. Millo, S. Silbert, I. Balberg, and N. Naghavi, Appl. Phys. Lett. **86**, 212102 (2005).

[14] B. Wang, J. Min, Y. Zhao, W. Sang, and C. Wang, Appl. Phys. Lett. **94**, 192101 (2009).

[15] C. Persson and A. Zunger, Phys. Rev. Lett. **91**, 266401 (2003).

[16] W. K. Metzger and M. Gloeckler, J. Appl. Phys. **98**, 063701 (2005).

[17] D. Azulay, O. Millo, I. Balberg, H. W. Schock, I. Visoly-Fisher, and D. Cahen, Sol. Energy Mater. Sol. Cells **91**, 85 (2007).

[18] V. Consonni, G. Feuillet, and P. Gergaud, J. Appl. Phys. **103**, 063529 (2008).

[19] C. V. Thompson and H. I. Smith, Appl. Phys. Lett. **44**, 603 (1984).

[20] V. Consonni and G. Feuillet, J. Appl. Phys. **105**, 083535 (2009).

[21] C. V. Thompson, J. Appl. Phys. **58**, 763 (1985).

[22] M. Hillert, Acta Mater. **47**, 4481 (1999).

[23] D. E. Cooper, J. Bajaj, and P. R. Newman, J. Cryst. Growth **86**, 544 (1988).

[24] J. M. Francou, K. Saminadayar, and J. L. Pautrat, Phys. Rev. B **41**, 12035 (1990).

[25] H. Y. Shin and C. Y. Sun, J. Cryst. Growth **186**, 354 (1998).

[26] D. M. Hofmann, P. Omling, H. G. Grimmeiss, B. K. Meyer, K. W. Benz, and D. Sinerius, Phys. Rev. B **45**, 6247 (1992).

[27] S. Seto, A. Tanaka, F. Takeda, and K. Matsuura, J. Cryst. Growth **138**, 346 (1994).

[28] T. A. Kuhn, W. Ossau, A. Waag, R. N. Bicknell-Tassius, and G. Landwehr, J. Cryst. Growth **117**, 660 (1992).

[29] V. Consonni, G. Feuillet, and S. Renet, J. Appl. Phys. **99**, 053502 (2006).

[30] Y. F. Yan, M. M. Al-Jassim, and T. Demuth, J. Appl. Phys. **90**, 3952 (2001).

[31] D. J. Dunstan, B. Gil, and K. P. Homewood, Phys. Rev. B **38**, 7862 (1988).

[32] P. Peyla, Y. Merle d'Aubigné, A. Wasiela, R. Romestain, H. Mariette, M. D. Sturge, N. Magnea, and H. Tuffigo, Phys. Rev. B **46**, 1557 (1992).

[33] Y. Merle d'Aubigné, H. Mariette, N. Magnea, H. Tuffigo, R. T. Cox, G. Lentz, Le Si Dang, J.-L. Pautrat, and A. Wasiela, J. Cryst. Growth **101**, 650 (1990).

[34] D. G. Thomas, J. Appl. Phys. **32**, 2298 (1961).

[35] M. Zigone, H. Roux-Buisson, H. Tuffigo, N. Magnea, and H. Mariette, Semicond. Sci. Technol. **6**, 454 (1991).

[36] J. P. Hirth and J. Lothe, *Theory of Dislocations* (Wiley, New York, 1982).

[37] A. A. Nazarov, A. E. Romanov, and R. Z. Valiev, Acta Metall. **41**, 1033 (1993).

[38] N. E. Christensen, S. Satpathy, and Z. Pawlowska, Phys. Rev. B **36**, 1032 (1987).

[39] A. Dal Corso, R. Resta, and S. Baroni, Phys. Rev. B **47**, 16252 (1993).

[40] R. André, C. Deshayes, J. Cibert, Le Si Dang, S. Tatarenko, and K. Saminadayar, Phys. Rev. B **42**, 11392 (1990).

[41] F. Greuter and G. Blatter, Semicond. Sci. Technol. **5**, 111 (1990).

[42] A. N. Pikhtin and A. D. Yas'kov, Sov. Phys. Semicond. **22**, 613 (1988).

[43] R. Spolenak, W. L. Brown, N. Tamura, A. A. MacDowell, R. S. Celestre, H. A. Padmore, B. Valek, J. C. Bravman, T. Marieb, H. Fujimoto, B. W. Batterman, and J. R. Patel, Phys. Rev. Lett. **90**, 096102 (2003).

[44] M. A. Phillips, R. Spolenak, N. Tamura, W. L. Brown, A. A. MacDowell, R. S. Celestre, H. A. Padmore, B. W. Batterman, E. Arzt, and J. R. Patel, Microelectron. Eng. **75**, 117 (2004).

[45] A. Krtschil, A. Dadgar, N. Oleynik, J. Bläsing, A. Diez, and A. Krost, Appl. Phys. Lett. **87**, 262105 (2005).

[46] F. Bertram, D. Forster, J. Christen, N. Oleynik, A. Dadgar, and A. Krost, Appl. Phys. Lett. **85**, 1976 (2004).

[47] R. D. Doherty, D. A. Hughes, F. J. Humphreys, J. J. Jonas, D. J. Jensen, M. E. Kassner, W. E. King, T. R. McNelley, H. J. McQueen, and A. D. Rollett, Mater. Sci. Eng., A **238**, 219 (1997).

[48] K. Lücke and G. Gottstein, Acta Metall. **29**, 779 (1981).

[49] Y. Estrin and K. Lücke, Acta Metall. **29**, 791 (1981).

[50] Y. Estrin, G. Gottstein, and L. S. Shvindlerman, Acta Mater. **47**, 3541 (1999).

[51] D. Berlincourt, H. Jaffe, and L. R. Shiozawa, Phys. Rev. **129**, 1009 (1963).

[52] A. Dal Corso, M. Posternak, R. Resta, and A. Baldereschi, Phys. Rev. B **50**, 10715 (1994).

[53] F. Bernardini, V. Fiorentini, and D. Vanderbilt, Phys. Rev. B **56**, R10024 (1997).

[54] S. de Gironcoli, S. Baroni, and R. Resta, Phys. Rev. Lett. **62**, 2853 (1989).

[55] D. Shvydka, J. Frayton, A. D. Compaan, and V. G. Karpov, Appl. Phys. Lett. **87**, 123505 (2005).